



Fabrication of all-solid-state textile supercapacitors based on industrial-grade multi-walled carbon nanotubes for enhanced energy storage

Rui S. Costa^{1,2} , Alexandra Guedes³ , André M. Pereira² , and Clara Pereira^{1,*}

¹REQUIMTE/LAQV, Departamento de Química e Bioquímica, Faculdade de Ciências, Universidade do Porto, Rua do Campo Alegre s/n, 4169-007 Porto, Portugal

²IFIMUP – Instituto de Física de Materiais Avançados, Nanotecnologia e Fotónica, Departamento de Física e Astronomia, Faculdade de Ciências, Universidade do Porto, 4169-007 Porto, Portugal

³Centro de Geologia e Departamento de Geociências, Ambiente e Ordenamento do Território, Faculdade de Ciências, Universidade do Porto, 4169-007 Porto, Portugal

Received: 18 January 2020

Accepted: 18 April 2020

Published online:

4 May 2020

© Springer Science+Business Media, LLC, part of Springer Nature 2020

ABSTRACT

Textile supercapacitors (TESCs) are an emerging energy storage solution to power smart gadgets integrated on clothes. Herein, efficient solid-state TESC with different active areas (2–8 cm²) were produced based on cotton fabrics coated with industrial grade multi-walled carbon nanotubes (MWCNTs) as electrodes and a safe polyelectrolyte. The textile electrodes were fabricated by an optimized eco-friendly scalable dip-pad-dry process. The lowest electrical resistance (2.62 Ω cm⁻²) and most uniform coating of the electrodes were achieved using 10 mg mL⁻¹ CNTs dispersion and 8 dip-pad-dry steps. The TESC exhibited a specific capacitance of 8.01 F g⁻¹ (9.18 F cm⁻²) and high cyclability (5000 cycles). The energy and power densities were tuned by changing the electrode area: the largest TESC presented the highest energy density of 6.30 Wh kg⁻¹, which was 14× higher than those of other EDLC-type carbon-based TESC reported in the literature; the smallest TESC presented the highest power density of 2.72 kW kg⁻¹, being 49× higher than the values reported for comparable systems. Finally, a sensor was powered for 47 min by coupling two TESC in series (14 cm²). This work demonstrated the ability to produce efficient TESC using industrial grade MWCNTs by processes implemented in the Textile Industry, boosting technological transfer for high-tech applications.

Address correspondence to E-mail: clara.pereira@fc.up.pt

Introduction

The global market for wearable electronics has been growing at an accelerating pace, with a wide diversity of applications, namely on high-tech sportswear, healthcare, workwear, protection, military, fashion, among others [1, 2]. In 2016, this market was valued at \$70 billion globally, being forecast to grow at a compound annual growth rate (CAGR) of 132% until 2022, to address the needs of the Internet of Things Era.

In order to electrically supply intelligent functionalities integrated on clothes, energy storage systems combining flexibility, comfort, lightness and low toxicity with high energy and power densities are highly required [3, 4]. Electrochemical energy storage systems such as lithium-ion batteries and supercapacitors (SCs) are considered the most promising technologies to meet the energy demands of wearable electronic devices [3–5]. In particular, textile-based electrochemical supercapacitors (TESCs) emerged as potential energy storage candidates due to their high power density, fast charging, excellent cycling stability, long cycle life and eco-friendliness. TESC are already being developed at a laboratory-scale as fabrics [2–4, 6–11] or fibers/yarns [12–17] to electrically feed integrated wearable electronics. Several processes have been used to produce them, such as dip-coating, screen-printing and fiber spinning. The first two offer advantages in terms of implementation, processability costs and scaling-up, since unfunctionalized textile fabrics and the required equipment are readily available in the Textile Industry [3, 18, 19]. Moreover, they enable the incorporation of higher loadings of active materials [2–4, 20]. Both natural and synthetic fabrics, such as cotton and polyester, have been selected as substrates for TESC design, owing to their porosity/breathability, high surface area, lightness, stretchability and cost-effectiveness [2–4, 21].

In the last years, several types of materials have been incorporated in fabrics/fibers to produce textile-based electrodes, namely carbon-based (nano)materials, metal oxides and conducting polymers, in order to improve the electrochemical performance of TESC, such as their capacitance, energy and power densities [2, 4, 22–27]. These materials have an important role in the energy storage mechanism since they endow electrical conductivity, high surface area

and/or redox properties to the TESC [4, 24–26], leading to electric double-layer or pseudocapacitive-type SCs, respectively.

The recent progress on carbon-based (nano)materials holds great opportunities for the design of advanced flexible electrodes owing to their high electrical conductivity, large surface area, excellent mechanical properties, high chemical and thermal stability and wide range of operation temperatures [28–31]. In particular, single-walled and multi-walled carbon nanotubes (SWCNTs and MWCNTs, respectively) have been key components for the production of TESC [27, 30, 32, 33]. Hu et al. were among the first to report the fabrication of TESC using cotton sheet and woven polyester fabric as substrates, SWCNTs ink as electrode material and LiPF_6 as liquid electrolyte [21]. The cotton-based TESC reached a specific capacitance of 80 F g^{-1} at 20 mA cm^{-2} ; nevertheless, it relied on the use of a toxic electrolyte. Pasta et al. produced a TESC using cotton coated with SWCNTs as electrodes and an aqueous electrolyte (Li_2SO_4), which achieved a specific capacitance of $70\text{--}80 \text{ F g}^{-1}$ at 0.1 mA cm^{-2} [34].

Most of the TESC based on CNTs reported in the literature are typically based on SWCNTs or rely on the use of liquid electrolytes, which are still great constraints in terms of safety and costs towards their scale-up and industrial implementation. MWCNTs constitute a potential alternative owing to their lower manufacturing costs (500 times lower) [35]. For instance, Xu et al. reported on the fabrication of a TESC composed of nonwoven cloth coated with hydroxyl-functionalized MWCNTs (or $\text{MnO}_2/\text{MWCNT}$) as electrodes and a liquid electrolyte (Na_2SO_4) [36]. However, the specific capacitance was only 16.40 mF cm^{-2} at 1 mA cm^{-2} with a single SC cell. Furthermore, no optimization of the concentration of the CNT dispersion was attempted, which is an important aspect to achieve enhanced performance. The performance could be improved by electrodeposition of MnO_2 on the CNT-coated cloth and/or by stacking multiple cells in a laminated or tandem configuration (using a liquid or solid-gel electrolyte, respectively). For instance, the authors were able to power four LED digital screens connected in series with 10 V output using the MnO_2 -based device with tandem structure composed of ten individual cells. However, no information on the maximum time the devices could be powered was reported.

Despite this progress, a systematic study of complementary specifications related with the TESC fabrication process itself is still lacking. In particular, no study concerning the optimization of the CNTs concentration in the dyeing dispersion to improve the textile electrode properties has been reported nor on the role of the electrode features on the energy storage properties of the resulting TESCs. The use of cost-effective industrial grade MWCNTs as well as of scalable eco-sustainable manufacturing processes for the fabrication of TESCs is also of major importance, aiming to boost the scale-up and implementation in the Textile Industry.

In view of these requirements, in this work, efficient all-solid-state TESCs based on industrial grade MWCNTs were produced through an optimized scalable cost-effective and eco-sustainable dip-pad-dry process that mimics those used for dyeing in the Textile Industry. To achieve that goal, fabric electrodes with different dimensions were firstly produced through the coating of a cotton substrate with MWCNTs. The influence of the concentration of the CNTs dispersion bath and of the number of dip-pad-dry steps on the electrical conductivity, coating homogeneity and MWCNTs loading of the resulting textile electrodes was assessed, towards reaching the best compromise between the three properties. Afterwards, the textile electrodes were assembled with a safe solid-gel electrolyte, in a sandwich-type configuration, to produce TESCs with different dimensions. We endeavor unveiling the role of the electrode features, namely geometrical features, electrode active area and nanomaterial loading on the energy storage properties of the resulting TESCs. This work constitutes a step forward on the understanding of the relationship between the electrode properties, the energy storage output (specific capacitance, energy/power density, internal resistance) and the cycle life of textile SCs towards scaling-up for industrial applications.

Materials and methods

Materials, reagents and solvents

The woven fabric, 100% cotton prepared for dyeing (warp: 3726, weft: 52 threads), was provided by Arco Têxteis S.A. (Portugal). The solvents toluene and absolute ethanol (both of analytical grade) and *ortho*-

phosphoric acid (H_3PO_4 , 85%, analytical grade) were purchased from Fisher Chemical. The commercial MWCNTs Nanocyl® NC7000™ (industrial grade) were supplied by Nanocyl S.A. According to the supplier, the MWCNTs have an average diameter of 9.5 nm, an average length of 1.5 μm and a surface area of 250–300 $\text{m}^2 \text{g}^{-1}$. Sodium dodecylbenzenesulfonate (SDBS) and poly(vinyl alcohol) (PVA, 99%) were acquired from Sigma-Aldrich. Ultrapure water (Millipore, specific resistivity: 18 $\text{M}\Omega \text{cm}$) was used throughout the experiments.

Cotton textiles coating with MWCNTs

In order to fabricate the textile electrodes, three aqueous MWCNT-based inks with concentrations of 5, 10 and 15 mg mL^{-1} were firstly prepared through dispersion of the MWCNTs into an SDBS aqueous solution, under sonication during 150 min. The resulting dispersions remained stable over long periods of time (more than 1 year).

Prior to the coating process, the woven cotton substrates ($8 \times 8 \text{ cm}^2$; average weight of 0.34 g) were sequentially washed with toluene, absolute ethanol and Millipore water and then dried at room temperature overnight. The coating of the cotton fabrics with the MWCNTs was performed through a dip-pad-dry process. Firstly, the cotton substrate was dipped into the MWCNTs dispersion and then submitted to a padding process in order to squeeze out the excess of CNTs. Finally, the resulting coated fabric was dried at 100 °C for 12 min. The dip-pad-dry process was repeated several times in order to increase the CNTs loading in the fabric and improve its electrical conductivity with the ultimate goal of optimizing the textile electrode properties.

Fabrication of all-solid-state textile SCs

The all-solid-state TESCs were fabricated in a multi-layer configuration (sandwich-type) through the assembly of two MWCNT-coated fabric electrodes (produced in “Cotton textiles coating with MWCNTs” section) using PVA– H_3PO_4 as solid-gel electrolyte. The solid-gel electrolyte was prepared by mixing H_3PO_4 and PVA (1:1 weight ratio) in 60 mL of Millipore water and heating to 90 °C under continuous stirring until the solution became clear.

Afterwards, two strips of MWCNT-coated cotton were coated with the electrolyte solution followed by

partial air-drying and then pressed together face-to-face to produce the solid-state TESC with the desired overlapping area. Four TESCs with electrode active surface areas (length \times width) of 1×2 , 2×2 , 1.5×4 and 2×4 cm² (overlapped area) were produced. The resulting TESCs will be denoted as TSC_X, with TSC_1, TSC_2, TSC_3 and TSC_4 corresponding to TESCs with active surface areas of 2, 4, 6 and 8 cm², respectively.

Physicochemical characterization

Scanning electron microscopy (SEM) and energy-dispersive X-ray spectroscopy (EDS) were performed at Centro de Materiais da Universidade do Porto (CEMUP), Portugal, using a high-resolution environmental scanning electron microscope (FEI Quanta 400 FEG ESEM) equipped with an energy-dispersive X-ray spectrometer (EDAX Genesis X4M). Transmission electron microscopy (TEM) was performed at Instituto de Investigação e Inovação em Saúde (i3S), Portugal, on a JEOL JEM 1400 microscope operating at an accelerating voltage of 120 kV and equipped with a CCD digital camera Orious (1100 W).

X-ray photoelectron spectroscopy (XPS) was performed at CEMUP, Portugal, on a Kratos AXIS Ultra HAS spectrometer equipped with a monochromatic Al K α X-ray source (1486.7 eV), operating at 15 kV (90 W) in fixed analyzer transmission (FAT) mode, with a pass energy of 80 eV for the survey spectra (1.0 eV step size) and 40 eV for the regions of interest (0.1 eV step size). The XPS spectra were deconvoluted with the CasaXPS software, using nonlinear least squares fitting routine after a Shirley-type background subtraction. The surface atomic percentages were calculated from the corresponding peak areas and using the sensitivity factors provided by the manufacturer.

The X-ray diffraction (XRD) measurements were performed at room temperature on a SmartLab Rigaku diffractometer operated at 9 kW power (40 kV and 200 mA), using Cu K α radiation ($\lambda = 1.5406$ Å) and Bragg–Brentano $\theta/2\theta$ configuration in the 2θ range of 10° – 90° , with an increase of 0.02° and scan rate of 10° min⁻¹.

Raman spectroscopy was performed at two different wavelengths: $\lambda = 532$ and 633 nm. In the case of the Raman characterization at $\lambda = 532$ nm, a Jobin–Yvon Xplora spectrometer (Horiba Scientific) with a laser power of 25 mW was used, while for the

characterization at $\lambda = 633$ nm, the spectra were acquired on a Jobin–Yvon LabRaman spectrometer with a laser power of 20 mW. In both analyses, an optical microscope with a 50 \times objective lens was used to focus the laser beam on the samples, as well as to investigate the quality of the analyzed areas before and after the measurements. All Raman spectra were acquired at room temperature using laser power reduced 50% by a filter in order to avoid samples damage.

The electrical resistance of the textiles before and after each dip-pad-dry step was measured with a digital multimeter by the two-contact technique.

Electrochemical characterization

Cyclic voltammetry (CV) and galvanostatic charge/discharge (GCD) tests were performed to the TESCs in a standard two-electrode cell configuration using a Keithley 2400 sourcemeter. The CV curves were acquired at scan rates of 1, 5, 10, 20, 50 and 100 mV s⁻¹ and the GCD curves were obtained at 0.1, 0.5, 1 and 2 mA. Electrochemical impedance spectroscopy (EIS) was performed in the frequency range of 0.1 Hz–1 MHz with 0 V mean voltage and 5 mV amplitude on an Autolab PGSTAT 20 potentiostat (EcoChimie), using the FRA software. All electrochemical measurements were conducted at room temperature.

Results and discussion

Fabrication of CNT-coated textile electrodes

The textile electrodes were fabricated by coating woven cotton fabrics with MWCNTs through a dip-pad-dry process. To unveil the optimum concentration of MWCNTs in the ink for the dip-pad-dry process, three aqueous MWCNTs dispersions with concentrations of 5, 10 and 15 mg mL⁻¹ were firstly prepared. For each concentration, 5 dip-pad-dry steps were performed using cotton substrates with dimensions of 4×4 cm².

The variation of the loading of MWCNTs incorporated in the fabric (in weight percentage) and of the resulting electrical properties after each dip-pad-dry step is presented in Fig. 1a, b, respectively. For all the tested MWCNT concentrations, the percentage of incorporated CNTs increases almost linearly with the

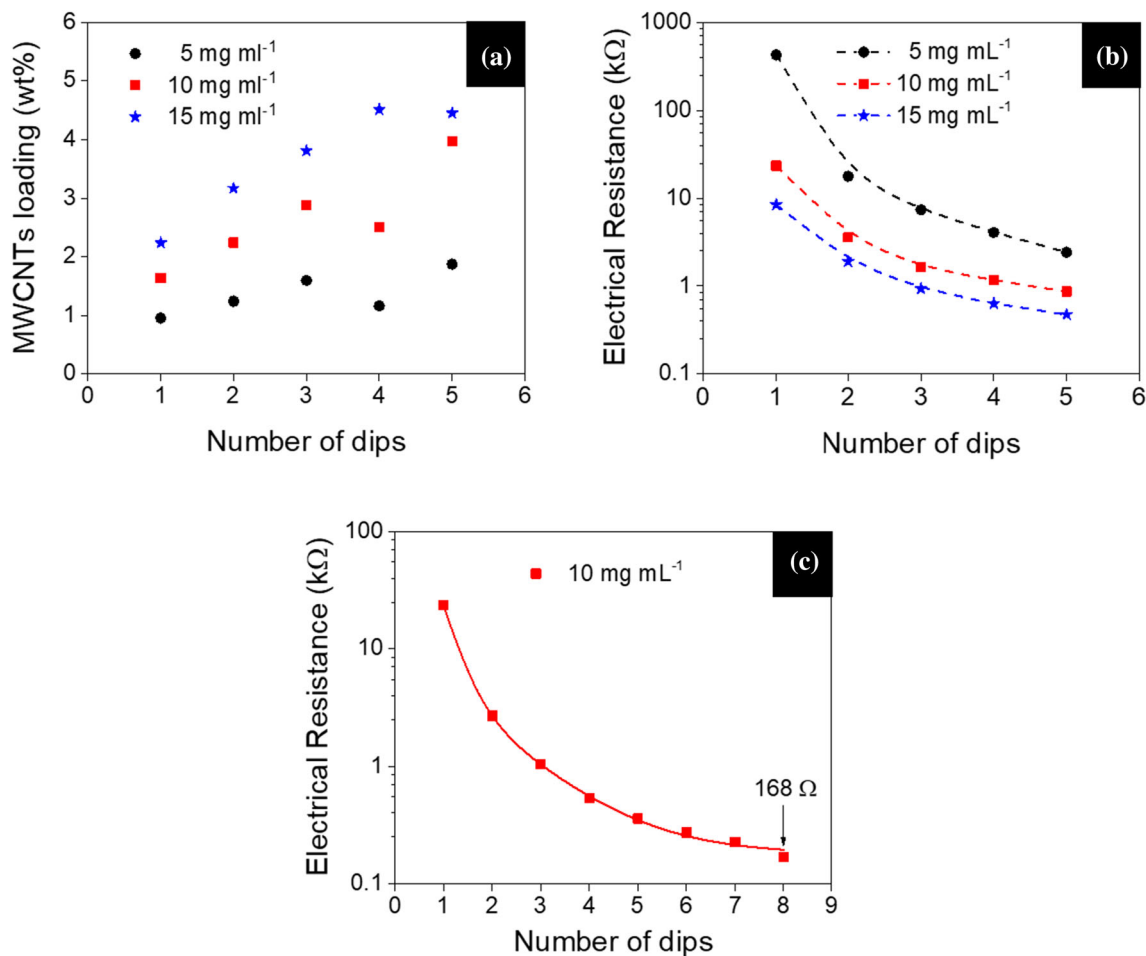


Figure 1 **a** Amount of incorporated MWCNTs (in wt%) and **b** electrical resistance of the CNT-coated cotton fabrics ($4 \times 4 \text{ cm}^2$) as a function of the number of dip-pad-dry steps, that were fabricated using MWCNTs dispersions with concentrations of 5,

10 and 15 mg mL^{-1} . **c** Electrical resistance of the $8 \times 8 \text{ cm}^2$ cotton fabric coated with the 10 mg mL^{-1} MWCNTs dispersion vs. the number of dips upon scale-up, until a total of 8 dip-pad-dry steps.

number of dip-pad-dry steps. In particular, the average amount of incorporated MWCNTs after each dip-coating step is 1.37, 2.64 and 3.63 wt\% for the fabrics coated with the $5, 10$ and 15 mg mL^{-1} dispersions, respectively. Furthermore, after each dip-coating step, the higher the concentration of MWCNTs in the dispersion used to coat the fabric, the higher the MWCNTs loading in the resulting textile substrate.

Concerning the variation of the electrical properties, for the three MWCNTs concentrations, the electrical resistance of the coated textiles decreases three orders of magnitude with the number of dips, thus leading to an enhancement of their electrical conductivity (Fig. 1b). For instance, the electrical resistance of the MWCNT-coated textile fabricated using the 10 mg mL^{-1} dispersion decreases from $23 \text{ k}\Omega$ to

860Ω after 5 dip-pad-dry steps, which corresponds to a resistance reduction of 96.3%. Similar trends were reported by Hu et al. [21], Yu et al. [37] and Xu et al. [36] for textile fabrics coated with CNTs or graphene, where a decrease of the fabrics resistance (and, concomitantly, an increase of their electrical conductivity) with the increase of the number of dips was observed.

Herein, the ink concentration of 15 mg mL^{-1} leads to the highest resistance reduction of the coated textile, reaching 475Ω after 5 dip-pad-dry steps, which corresponds to an electrical resistivity (ρ) of $7.45 \Omega\text{-cm}$, obtained by the following equation:

$$\rho = R \frac{A}{l} \tag{1}$$

where R is the electrical resistance after 5 dip-pad-dry steps (in Ω), A is the area of the fabric substrate (in cm^2) and l is the length of the fabric substrate (in cm). However, when scaling-up the 15 mg mL^{-1} MWCNTs ink production, a poor MWCNTs dispersion was obtained; in contrast, the less concentrated inks led to reproducible values upon scale-up. For this reason and since the tendency of the graphs presented in Fig. 1a, b corresponding to the ink concentrations of 10 and 15 mg mL^{-1} are approximately equal, a scale-up experiment was performed with the 10 mg mL^{-1} ink using a cotton substrate four times larger (64 cm^2 vs. 16 cm^2) and a higher number of dip-pad-dry steps (8 steps). As can be observed from Fig. 1c, the resistance of the coated textile reaches the minimum value of 168Ω after 8 steps (electrical resistivity of $2.64 \Omega\text{-cm}$), thus being achieved a percolation state.

Therefore, for the production of the TESCs, the 10 mg mL^{-1} MWCNTs ink was selected and a total of 8 dip-pad-dry steps was performed. The resulting coated textile (denoted as CNT@Cotton fabric) presents a black and homogeneous color, which confirms the successful incorporation of the MWCNTs (inset of Fig. 2c vs. inset of Fig. 2a for the pristine cotton sample). Furthermore, it can be highlighted that the increase of the textile weight after the MWCNTs coating was only of 3.79 wt%, thus preserving its lightness.

The topology of the textiles surface before and after the MWCNTs incorporation was characterized by SEM (Fig. 2). The SEM images show that the parent cotton fabric consists of interwoven fibers with a smooth surface and a diameter in the range of 12–16 μm (Fig. 2a, b). The chemical composition of the parent cotton fabric, evaluated by EDS (Figure S1A in Supplementary Material) reveals the presence of carbon and oxygen, proving that the fabric is mainly composed of these elements that are characteristic of cellulose.

In order to obtain information about the morphology of the commercial MWCNTs prior to their incorporation on the cotton substrate, they were characterized by TEM. The corresponding TEM micrographs presented in Figs. 2f and S2 in Supplementary Material confirm the tubular morphology of the carbon nanotubes exhibiting both open and closed ends, as well as their random orientation. Moreover, they present average inner and outer

diameters of $4.8 \pm 1.1 \text{ nm}$ and $12.2 \pm 2.6 \text{ nm}$, respectively.

The SEM images of the MWCNT-coated cotton after 8 dip-coating steps (Fig. 2c, d) show that the cotton fabric was successfully coated with the CNTs, which are homogeneously distributed throughout the fibers surface. Additionally, the structure of the parent cotton fibers was preserved. The high-magnification SEM image of the coated fabric ($20,000\times$) presented in Fig. 2e reveals that the incorporated MWCNTs do not have a preferential direction, being randomly oriented throughout the cellulose fibers surface, which is in accordance with the TEM results of the pristine MWCNTs. The EDS analysis (Figure S1B in Supplementary Material) reveals that the carbon at% of the coated textile almost doubles when compared to that of the parent cotton fabric, due to the presence of the CNTs (Figure S1B vs. Figure S1A in Supplementary Material). In addition, small amounts of sodium and sulfur are detected, arising from the surfactant agent used in the CNTs dispersion.

The surface chemical composition of the cotton-based samples as well as of the parent MWCNTs was determined by XPS and the results are summarized in Table 1.

The parent cotton fabric is composed of carbon and oxygen, with surface atomic percentages of 61.7 and 38.3%, respectively. Furthermore, the high-resolution C 1s and O 1s spectra could be deconvoluted in the characteristic organic groups of cellulose (not shown). Upon the MWCNTs coating (CNT@Cotton sample), a significant increase in the carbon surface atomic percentage can be observed, as well as a decrease in the oxygen surface loading, leading to an O/C ratio of 0.064, which is similar to that obtained by EDS. This is in accordance with the surface chemical composition of the pristine MWCNTs, which are mainly composed of carbon (99.1%) and a trace amount of oxygen (0.9%). Additionally, sodium and sulfur from the dispersing agent were detected in the coated fabric, being present in similar amounts to those determined by EDS.

The XRD patterns of cotton and CNT@Cotton samples are illustrated in Fig. 3a. Both diffractograms present diffraction peaks at $2\theta = 14.9^\circ$, 16.7° , 22.8° and 34.1° that correspond to the $(1\bar{1}0)$, (110) , (020) and (004) reflections of cellulose, respectively, with a monoclinic crystal symmetry and space group $P2_1$

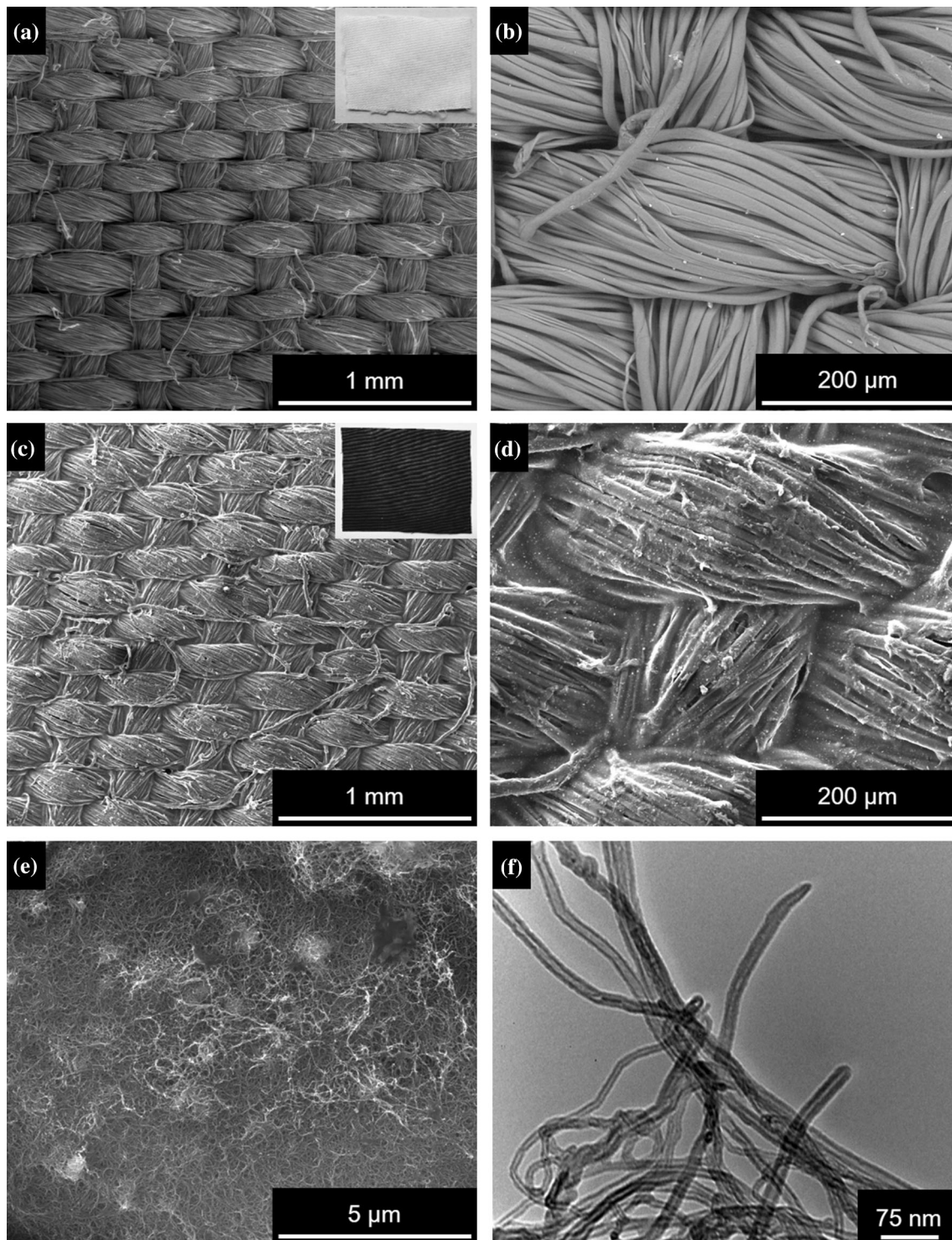
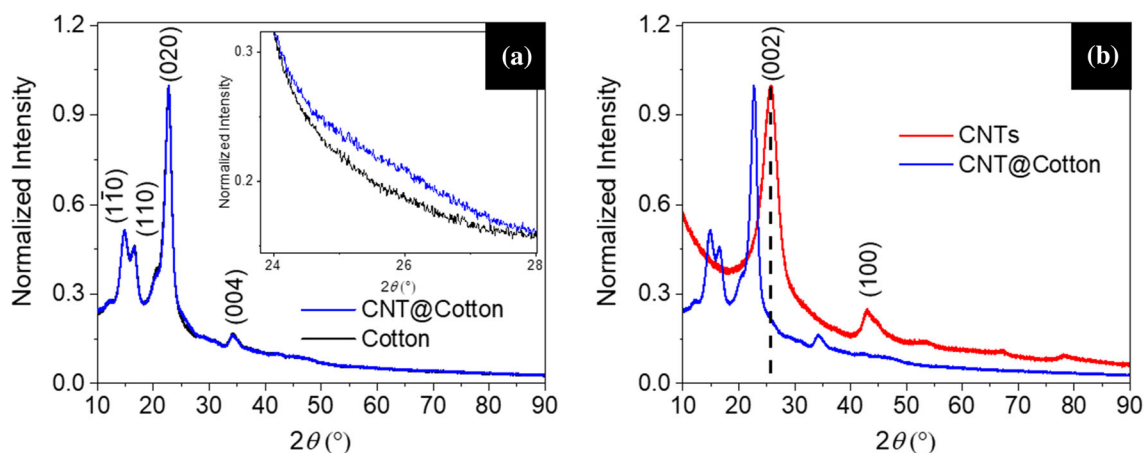


Figure 2 a, b SEM micrographs (105 \times and 500 \times magnification, respectively) of the parent cotton fabric. c–e SEM micrographs (105 \times , 500 \times and 20,000 \times magnification, respectively) of the

CNT@Cotton fabric. f TEM micrograph (250,000 \times) of the commercial MWCNTs. Insets of a and c: Digital photographs of the cotton fabric before and after MWCNTs incorporation.

Table 1 Surface atomic percentages of cotton-based samples and parent MWCNTs obtained by XPS^a

Sample	Atomic%				O/C			Na/C		S/C
	C 1s	O 1s	Na 1s	S 2p	XPS	EDS	XPS	EDS	XPS	EDS
Cotton	61.7	38.3	n.d. ^c	n.d. ^c	0.62	0.79	–	–	–	–
CNT@Cotton ^b	92.2	5.9	1.2	0.7	0.064	0.064	0.013	0.013	0.008	0.007
CNTs	99.1	0.9	n.d. ^c	n.d. ^c	0.009	–	–	–	–	–

^aDetermined by the areas of the respective bands in the high-resolution XPS spectra^b8 × 8 cm² sample, after 8 dip-pad-dry steps^cn.d. not detected**Figure 3** XRD patterns of **a** Cotton and CNT@Cotton samples and **b** parent MWCNTs and CNT@Cotton.

[38, 39]. Therefore, the incorporation of the MWCNTs in the cotton surface does not change the crystalline structure of the parent fabric.

In the diffractogram of CNT@Cotton fabric, it can be highlighted the appearance of a weak shoulder at $2\theta \approx 25.8^\circ$ (as shown in the inset of Fig. 3a), that corresponds to the most intense Bragg reflection of the parent MWCNTs (Fig. 3b). In fact, the XRD pattern of the MWCNTs features a strong diffraction peak at $2\theta = 25.7^\circ$ and an additional peak at $2\theta = 42.8^\circ$, that correspond to the (002) and (100) reflections of graphite, respectively [40].

In Fig. 4a are presented the Raman spectra of the parent MWCNTs and CNT@Cotton in the range of 1000–2000 cm^{-1} acquired with a $\lambda = 633$ nm laser. The Raman spectrum of the pristine cotton fabric could not be acquired at this wavelength due to the strong fluorescence of the sample [41]. The Raman spectrum of the parent MWCNTs exhibits two bands at 1319 and 1574 cm^{-1} , which correspond to the D and G bands of CNTs, respectively. The D band is associated with the double resonant Raman vibrations of the sp^2 atoms, being usually used to quantify

the structural disorder arising from amorphous carbon, while the G band corresponds to the tangential stretching vibrations of the carbon atoms [42, 43]. The spectrum of CNT@Cotton exhibits a similar profile, featuring the two characteristic D and G bands of the CNTs, at 1326 and 1589 cm^{-1} , respectively. However, both bands are shifted to higher wavenumbers when compared with the D and G bands of the MWCNTs spectrum (7 and 15 cm^{-1} shift for the D and G bands, respectively), suggesting the existence of interactions between the cotton fibers and the MWCNTs probably of non-covalent nature (e.g., hydrogen bonds) [44]. The ratio between the intensity of the D and G bands, I_D/I_G , can be used to compare the level of disorder of the carbon material structure [44]. The pristine MWCNTs and CNT@Cotton samples present comparable I_D/I_G values (1.80 vs. 1.78), indicating that the MWCNTs structure was preserved upon their incorporation on the cotton substrate.

Since the vibration modes associated with the cotton fabric could not be identified by Raman spectroscopy at $\lambda = 633$ nm, a complementary Raman study was performed using a $\lambda = 532$ nm laser

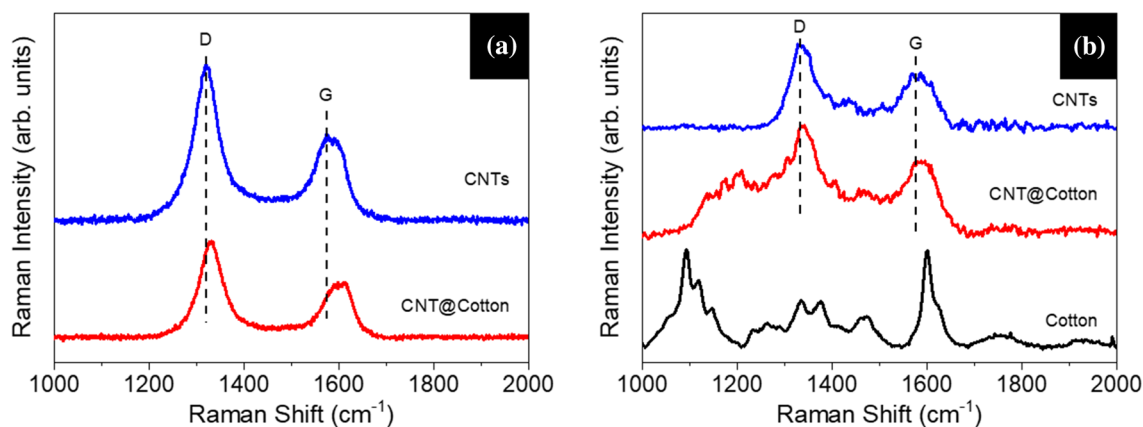


Figure 4 Raman spectra of **a** MWCNTs and CNT@Cotton acquired with $\lambda = 633$ nm laser and **b** MWCNTs, CNT@Cotton and Cotton acquired with $\lambda = 532$ nm laser.

(Fig. 4b). The Raman spectrum of the cotton fabric shows several bands/peaks associated with cellulose structure: at 1092, 1118 and 1147 cm^{-1} related to C–O–C glycosidic linkage asymmetric stretching, C–O–C glycosidic linkage symmetric stretching and C–C ring asymmetric stretching vibrations, respectively; at 1231 cm^{-1} , corresponding to C–O–H out-of-plane bending vibrations; at 1262 and 1285 cm^{-1} associated with CH_2 twisting vibrations; at 1335 cm^{-1} assigned to CH_2 bending vibrations; at 1376 cm^{-1} attributed to CH_2 , H–C–C, H–C–O and C–O–H bending vibrations; and, finally, a doublet at 1461 and 1477 cm^{-1} assigned to amorphous and crystalline cellulose, respectively [45, 46]. On the other hand, the Raman spectrum of the parent MWCNTs presents the characteristic D and G bands at 1333 and 1576 cm^{-1} , respectively. The Raman spectrum of CNT@Cotton exhibits the fingerprint vibration modes of both the cotton substrate and MWCNTs, confirming the presence of both components.

Hence, the morphological, chemical and structural characterization as well as the electrical properties of CNT@Cotton confirm that the incorporation of the MWCNTs onto the cotton substrate was successfully performed, with the cellulose fibers being completely coated with the MWCNTs and the fabric becoming electrically conductive.

Smart textile supercapacitors performance

Upon the characterization and optimization of the MWCNT-coated textile electrode properties, textile-based SCs with different active electrode areas (i.e., contact area between the electrodes and the

electrolyte) were produced, through the same scalable textile dyeing process, in order to unveil the role of the active area on the energy storage outputs of the resulting SCs (specific capacitance, equivalent series resistance, energy density and power density). In this context, four TESC with effective electrode areas ranging from 2 to 8 cm^2 were produced: TSC_1, TSC_2, TSC_3 and TSC_4, with active areas of 1×2 , 2×2 , 1.5×4 and 2×4 cm^2 (length \times width), respectively.

To achieve that goal, the MWCNT-coated cotton fabrics submitted to 8 dip-pad-dry steps using the 10 mg mL^{-1} MWCNT dispersion were directly used as electrodes for the fabrication of all-solid-state TESC with multilayer configuration (sandwich-type), using PVA– H_3PO_4 as solid-gel electrolyte (Figure S3 in Supplementary Material). The solid-gel polymer, besides contributing to the preservation of the flexibility of the TESC, had a dual function of electrolyte and separator, in order to avoid short circuits [2]. The CNT@Cotton fabrics were simultaneously used as electrodes and current collectors due to their high electrical conductivity.

The electrochemical performance of the TESC was evaluated by EIS, CV and GCD techniques, in a two-electrode configuration. This configuration was selected instead of the three-electrode system since it is more identical to real operation conditions of SC devices [5, 47, 48]. EIS was carried out for an in-depth understanding of the electrochemical behavior of the TESC as a function of frequency. In Fig. 5a are presented the Nyquist plots for the four devices with different effective electrode areas (2, 4, 6 and 8 cm^2) and the corresponding equivalent series resistance

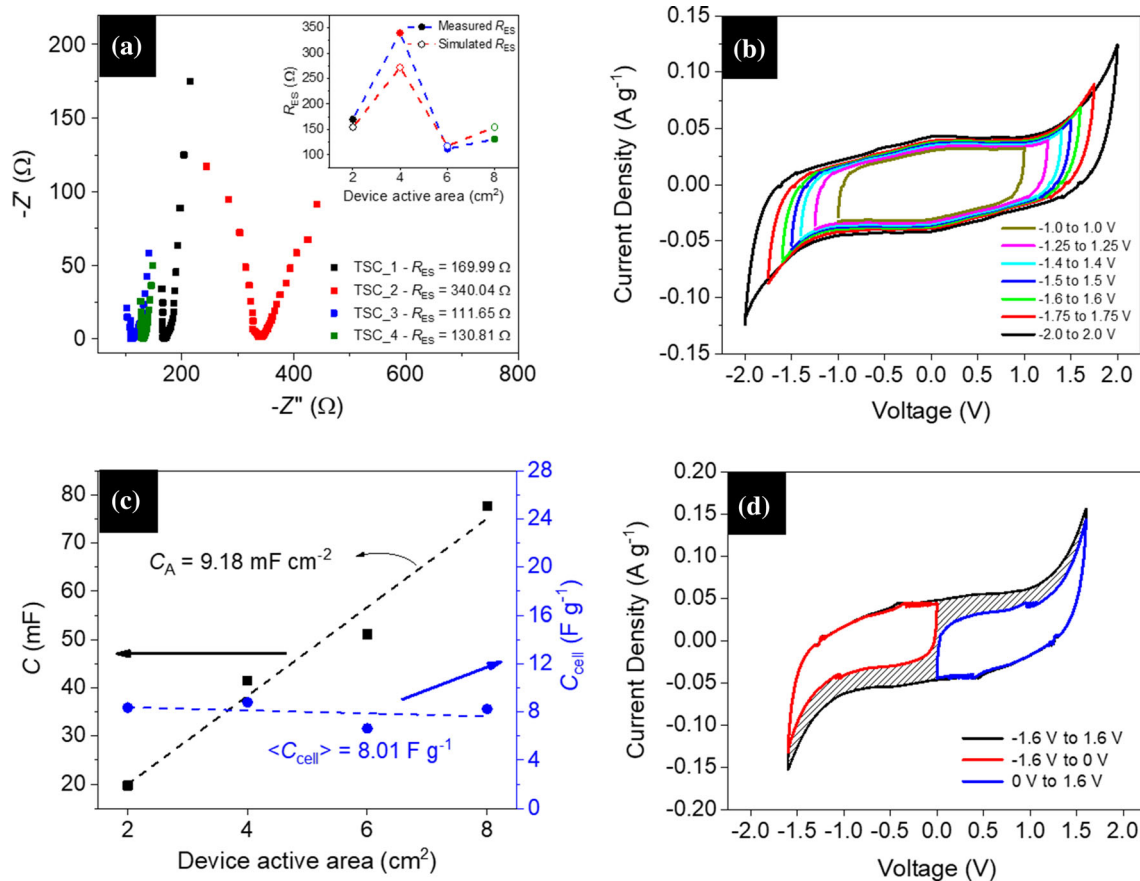


Figure 5 **a** Nyquist plots of the as-prepared TESCs in the frequency range of 0.1 Hz to 1 MHz. Inset: Difference between the R_{ES} experimentally obtained by EIS (measured R_{ES}) and the R_{ES} predicted through Eq. 1 (simulated R_{ES}). **b** Cyclic voltammograms of TSC_4 in different potential windows (from -1.0 V to 1.0 V until -2.0 V to 2.0 V) at a scan rate of 5 mV s^{-1} . **c** Non-normalized capacitance (C) and gravimetric specific capacitance (C_{cell}) as a function of active electrode area

(C_A is the areal capacitance determined through the slope of C vs. active electrode area relation; $\langle C_{\text{cell}} \rangle$ is the average gravimetric specific capacitance of the TESCs). **d** Comparison between the areas of the i - V cycles of TSC_1 acquired in the negative and positive ranges of the potential window (negative and positive half cycles, red and blue curves, respectively) vs. the area of the full i - V cycle (black curve), at a scan rate of 5 mV s^{-1} .

(R_{ES}) values (inset). Similar impedance profiles were observed for all TESCs, which can be divided into three parts: (1) a section of a semicircle curve at high frequencies, (2) a straight line with a slope of $\sim 45^\circ$ at medium frequencies, and (3) a quasi-vertical line at low frequencies [49]. The semicircle curve part at high frequencies is related with the electrodes and electrolyte resistances, the interfacial resistance between the electrolyte and the electrodes, and the contact resistance between the electrodes and the current collectors. The straight line with a slope of $\sim 45^\circ$, visible at intermediate frequencies, is known as Warburg impedance and is associated with the resistance to the electrolyte ions penetration and diffusion throughout the porous structure of the

electrodes. Finally, the vertical line at low frequencies is related with the pure capacitive behavior of the electric double-layer capacitor (EDLC) due to the electric double-layer formed at the electrode/electrolyte interfaces [49]. It is noteworthy that, at high frequencies, the Nyquist plots of all TESCs almost do not present the semicircle characteristic of faradaic charge transfer mechanisms (Fig. 5a), indicating the almost inexistence of redox reactions at the electrode/electrolyte interfaces [47, 50]. This feature is consistent with ultra-high rate capability and high power performance of EDLCs, unveiling that the energy storage mechanism that exists in the produced TESCs is non-faradaic (electrostatic process)

and, consequently, the SCs are of the EDLC-type [1, 4, 51].

The R_{ES} values were extracted from the real part of the complex impedance (Z') at 1 kHz [47] and are presented in Table 2 and as inset of Fig. 5a.

Considering that all devices were produced through a scalable manufacturing process, small R_{ES} values were obtained (111.65–340.04 Ω) due to the high electrical conductivity and high surface area of the incorporated CNTs. When the effective area of the electrodes increases, it is expected that the R_{ES} of the devices will also increase due to the increase in the interfacial contact resistance between the active electrode materials and the electrolyte [52]. However, the results show that the obtained R_{ES} values do not follow that tendency since the devices with larger area have lower R_{ES} than those with smaller area (111.65 Ω and 130.81 Ω for TSC_3 and TSC_4, respectively, vs. 169.99 Ω and 340.04 Ω for TSC_1 and TSC_2, respectively). To unveil the reason for this tendency, a geometrical factor was explored in order to assess if the electrodes shape can influence the overall performance of the devices. In this context, additional tests were performed with two TESCs with similar effective areas but with different length \times width dimensions (length measured longitudinally vs. width measured transversally), i.e., $1 \times 2 \text{ cm}^2$ and $2 \times 1 \text{ cm}^2$ (TSC_1 and TSC_5, respectively). The EIS results revealed that TSC_5 with $2 \times 1 \text{ cm}^2$ presents larger R_{ES} (246.80 Ω) than TSC_1 (169.99 Ω), confirming the influence of geometrical factors on the TESCs performance. To measure the equivalent series resistance through the EIS method, an AC voltage is applied between both

electrodes in a two electrodes configuration. Then, taking into account the geometry of each device, in TSC_1 ($1 \times 2 \text{ cm}^2$) the number of ions forming the electric double layer is larger (higher width value: 2 cm) and they have to travel a shorter distance (smaller length value: 1 cm) than in the case of TSC_5 ($2 \times 1 \text{ cm}^2$), giving rise to a smaller R_{ES} . These results thus confirm that, besides the total active area, a geometry factor needs to be taken into consideration to explain the R_{ES} tendency of the as-prepared devices: TSC_3 (111.65 Ω) < TSC_4 (130.81 Ω) < TSC_1 (169.99 Ω) < TSC_2 (340.04 Ω). In particular, the devices with larger width (4 cm, i.e., TSC_3 and TSC_4) are those that present lower restrictions to electrolyte ions diffusion. Moreover, when considering devices with similar width, the R_{ES} values increase with the increase of the length: TSC_3 ($1.5 \times 4 \text{ cm}^2$) < TSC_4 ($2 \times 4 \text{ cm}^2$) and TSC_1 ($1 \times 2 \text{ cm}^2$) < TSC_2 ($2 \times 2 \text{ cm}^2$).

To confirm the accuracy of the R_{ES} values obtained through EIS measurements, the theoretical R_{ES} of each device was calculated and is plotted in the inset of Fig. 5a along with the experimental ones. These values were obtained through Eq. 1, considering all TESCs as a system of two electrical resistances (two electrodes) in series with a capacitor (electrolyte) and using a reference resistivity value of 3.93 $\Omega \cdot \text{cm}$, which was calculated for a $1 \times 1 \text{ cm}^2$ MWCNT-coated cotton fabric prepared under similar conditions to those used in the preparation of all TESCs (10 mg mL⁻¹ MWCNTs dispersion, 8 dip-pad-dry steps). As can be observed from the inset of Fig. 5a, the theoretical R_{ES} values (154.48, 271.89, 117.41 and 154.48 Ω for TSC_1, TSC_2, TSC_3 and TSC_4, respectively) are

Table 2 Summary of the electrochemical parameters obtained for the four CNT-based TESCs with different effective electrode areas

Supercapacitor	Dimensions (cm \times cm)	m^a (mg)	R_{ES} (Ω)	C^b (mF)	C_{cell}^b (F g^{-1})	V_0^c (V)	$IR \text{ drop}^c$ (V)	I_{max} (mA)	E^d (W h kg ⁻¹)	P^d (kW kg ⁻¹)
TSC_1	1×2	2.36	169.99	19.70	8.35	2.09	0.45	12.29	5.07	2.72
TSC_2	2×2	4.72	340.04	41.50	8.79	2.17	1.20	6.38	5.77	0.74
TSC_3	1.5×4	7.71	111.65	51.13	6.63	2.39	1.26	21.41	5.29	1.67
TSC_4	2×4	9.44	130.81	77.72	8.24	2.35	1.24	17.96	6.30	1.12

^aTotal effective electrodes mass (including positive and negative electrodes)

^bNon-normalized capacitance (C) and gravimetric specific capacitance (C_{cell}) of the SC cell at a scan rate of 5 mV s⁻¹, calculated by Eqs. (2) and (3), respectively

^cObtained by GCD technique

^dEnergy density and power density values at a scan rate of 5 mV s⁻¹, calculated by Eqs. (5) and (6), respectively

comparable to those obtained experimentally, showing that the results obtained by EIS are accurate.

In order to determine the maximum working potential window for this type of devices, cyclic voltammograms of the TESC device with the largest area (TSC_4) were acquired in several potential windows at a scan rate of 5 mV s^{-1} (Fig. 5b): -1.0 – 1.0 V , -1.25 to 1.25 V , -1.4 to 1.4 V , -1.5 to 1.5 V , -1.6 to 1.6 V , -1.75 to 1.75 V and -2.0 to 2.0 V . For all potential windows, the CV curves show a nearly rectangular shape which confirms that the SC presents an ELDC-type behavior [12, 53], in accordance with the results obtained by EIS. Nevertheless, for potential windows higher than -1.6 to 1.6 V , the CV curves become distorted at the edges, with peaks being observed at the end of the i - V cycles due to the decomposition of water (electrolysis) [54]. In this context, these devices present a stable operation behavior until a maximum working voltage of 1.6 V , which is in accordance with the characteristics of the selected solid-gel electrolyte that typically features a working voltage between 1 and 2 V [55]. In Figure S4 (Supplementary Material) are presented the cyclic voltammograms of all four textile devices in the potential window of -1.6 to 1.6 V , acquired at a scan rate of 5 mV s^{-1} . All i - V cycles are nearly rectangular and symmetric, which is a signature of a stable electrochemical performance [6, 53, 56]. The charge storage mechanism of all the prepared TESCs thus relies on the occurrence of reversible adsorption/desorption of electrolyte ions at the surface and/or within the pores of the electrode material, thus being a purely electrostatic process (non-faradaic) characteristic of EDLCs [4, 57].

The non-normalized capacitance (C) and the gravimetric specific capacitance (C_{cell}) values of the fabricated TESC cells, expressed in mF and F g^{-1} , respectively, were calculated from the CV curves at 5 mV s^{-1} presented in Figure S4 (Supplementary Material) using the following equations [47, 48]:

$$C = \frac{1}{2v\Delta V} \int_{V_-}^{V_+} I(V)dV \quad (2)$$

and

$$C_{\text{cell}} = \frac{1}{2mv\Delta V} \int_{V_-}^{V_+} I(V)dV \quad (3)$$

where m is the total mass of active material in both electrodes (expressed in grams), v is the scan rate (in

V s^{-1}), ΔV is the potential window (in V), I is the current intensity (in A) and V_- and V_+ are the applied voltage limits (in V).

The obtained C and C_{cell} values are summarized in Table 2. Moreover, the variation of both C and C_{cell} as a function of the effective electrode area of the TESCs is presented in Fig. 5c. The results show that the non-normalized capacitance increases linearly upon the increase of the electrode area. The areal capacitance can be extracted through the slope of the linear relation, presenting a value of 9.18 mF cm^{-2} . On the other hand, the gravimetric specific capacitance is practically constant for all TESCs, regardless of the corresponding effective electrode areas, with a mean value of $\langle C_{\text{cell}} \rangle = 8.01 \pm 0.67 \text{ F g}^{-1}$.

In order to study the capacitive behavior of the TESCs in the positive and negative ranges of the potential window, CV measurements were performed from -1.6 to 0 V and from 0 to 1.6 V (half cycles) at a scan rate of 5 mV s^{-1} for the device with the smallest area (TSC_1). In Fig. 5d are plotted the corresponding i - V curves of the half cycles and that of the full cycle (from -1.6 to 1.6 V) at similar scan rates, with the difference between the cycle areas highlighted by a dashed shadow. The results show that both half cycles are nearly symmetrical, leading to specific capacitances of 5.87 and 6.14 F g^{-1} for the semi-negative and semi-positive cycles, respectively, and a total capacitance of 12.01 F g^{-1} , obtained by summing both individual values. However, the specific capacitance of the full cycle (from -1.6 to 1.6 V) is 8.35 F g^{-1} , which is 1.4 times lower than the total capacitance obtained by summing the specific capacitances of both half-semi cycles (12.01 vs. 8.35 F g^{-1}). This difference can be explained by the occurrence of some discharge phenomenon upon reversing the applied voltage when the devices are measured in the full potential window (from -1.6 to 1.6 V). Similar results were verified for all devices (not shown).

To explore the scan rate effects on the C_{cell} of the TESCs, CV measurements at different scan rates were performed for the smallest and the largest TESCs (TSC_1 and TSC_4, respectively). In Figure S5 (Supplementary Material) is presented the variation of the C_{cell} of both devices at different scan rates normalized by the corresponding C_{cell} at 1 mV s^{-1} (C_{cell}/C_0) as a function of the scan rate ($1, 5, 10, 25, 50, 75$ and 100 mV s^{-1}). In both cases, regardless of the SC area, the cell specific capacitance is higher at lower scan

rates because the electrolyte ions have more time to penetrate and reside within the available pores of the electrode material and thus form the electric double layer which is necessary to generate high capacitance, being in accordance with the literature [53, 58].

GCD measurements were performed to determine the working voltage and the *IR* drop of the TESCs (defined below). The measurements were performed in two steps using a similar charging time for direct comparison between all devices: in the first 60 s the voltage of the SCs was measured with an applied current density of 1 A g⁻¹ (SCs charge) and, in the following 60 s, the working voltage was monitored without any current being applied (SCs discharge at open circuit). The GCD curves of all four devices, presented in Fig. 6a, exhibit similar behavior, with the voltage increase being more pronounced in the first charging seconds because the electrodes active

area available for the diffusion of the electrolyte ions is larger; then, after 20–25 s, the devices voltage begins to saturate. When the current is no longer applied (after 60 s), a sudden decrease of the voltage of the devices occurs. The first voltage value measured after switching off the applied current is defined as the working voltage of the SC (*V*₀), while the difference between that value and the last voltage measured before switching off the applied current is defined as the voltage drop (*IR* drop, see inset of Fig. 6a) [47]. This voltage drop is expectable and is associated with the internal resistance of the devices, which arises from the limited diffusion mobility of the electrolyte ions within the electrodes structure [8, 47, 59]. The devices present working voltages between 2.09 V for the smallest one (TSC_1, see Table 2) and 2.39 V and 2.35 V for the devices with 6 and 8 cm², respectively (TSC_3 and TSC_4). In this

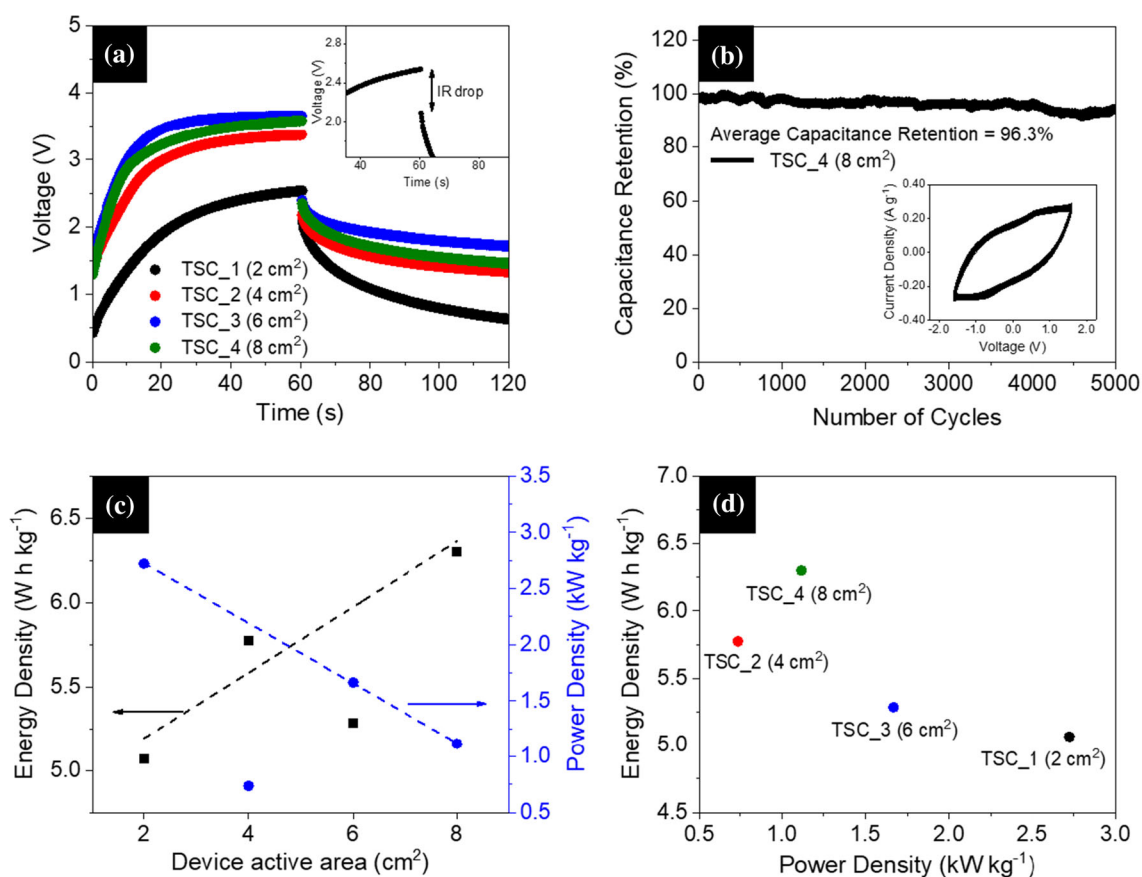


Figure 6 a GCD curves of the four TESCs prepared in this work obtained at a current density of 1 A g⁻¹ during the charging process (60 s) and with no applied current during the discharge process (next 60 s). Inset: *IR* drop obtained for TSC_1. b Cycling stability test for the TESC with active electrode area of 8 cm²

during 5000 cycles. The inset shows the respective *i-V* cycles during 5000 cycles. c Energy density and power density as a function of the active electrode area for the four TESCs. d Ragone plot for the four TESCs with different electrode areas (2, 4, 6 and 8 cm²).

sense, for the same charging time (60 s), at a similar current density of 1 A g^{-1} , the working voltage of the TESC initially increases with the increase of the electrode active area until reaching 6 cm^2 and then remains practically constant (Table 2).

For a deeper understanding of the behavior of the TESC during the charge and discharge processes, they were charged at different current densities ($I = 0.2, 0.4, 0.6, 0.8$ and 1 A g^{-1}) and discharged at open circuit during the same period of time (60 s). In Figure S6 (Supplementary Material) are presented all GCD curves, being possible to observe that as the current density increases, the devices voltage reaches saturation more rapidly. Moreover, for all devices, at high values of current density ($0.6, 0.8$ and 1 A g^{-1}), the discharge curves are almost overlapping, suggesting that, for each device, the working voltage reaches a maximum value at a certain current density and then remains constant despite the increase of the charging current; this suggests that regardless of the TESC area, the increase in the current density during charging only accelerates the charging process of the devices, with no influence on the V_0 values.

The determination of the V_0 and R_{ES} values allows estimating the maximum supplied current of each device (I_{\max} , in A) through Ohm's law:

$$I_{\max} = \frac{V_0}{R_{ES}} \quad (4)$$

The devices present maximum current intensities (Table 2) ranging from 6.38 mA for the device with $2 \times 2 \text{ cm}^2$ (TSC_2) and 21.41 mA for the device with $1.5 \times 4 \text{ cm}^2$ (TSC_3). Moreover, it is noteworthy that the I_{\max} values follow the inverse tendency of the R_{ES} results, which suggests that R_{ES} is the main factor that determines I_{\max} since all devices present comparable V_0 values.

The cycling stability of all TESC, i.e., the number of charge/discharge cycles that they are able to withstand without significant decrease in the specific capacitance, was evaluated by performing 5000 consecutive i - V cycles. As example, in Fig. 6b are depicted the results for the $2 \times 4 \text{ cm}^2$ TESC (TSC_4), showing that its specific capacitance upon multiple charge/discharge cycles only slightly decreases in the first 800 cycles and then remains almost constant, with an average capacitance retention of 96.3% for up to 5000 cycles. This certifies the high cycling stability, thus confirming that the combination of industrial grade MWCNTs electrode material with the solid-gel

polymer electrolyte and the straightforward fabrication process is an appealing choice for the development of robust textile SCs.

Among all performance metrics for energy storage, energy density and power density of the whole SC cell are the most relevant parameters for end-user applications and hence are the most often used for SC performance evaluation [2, 47, 60]. The energy density (E , W h kg^{-1}) and the power density (P , W kg^{-1}) of the assembled TESC were calculated by the following equations [47, 48]:

$$E = \frac{1}{2 \times 3.6} C_{\text{cell}} V_0^2 \quad (5)$$

$$P = \frac{V_0^2}{4R_{ES}m} \quad (6)$$

where m is the total mass of active materials in both electrodes (in kg) and with the C_{cell} values being expressed in F g^{-1} .

In Fig. 6c is plotted the variation of the energy and power densities of the four devices as a function of the corresponding effective electrode areas. In general, the energy density increases upon the increase of the electrode area (except for TSC_3), while the power density decreases (except for TSC_2). In particular, the energy density values of the TESC vary between 5.07 W h kg^{-1} (TSC_1, smallest area) and 6.30 W h kg^{-1} (TSC_4, largest area) and the power density values change between 0.74 kW kg^{-1} (TSC_2) and 2.72 kW kg^{-1} (TSC_1) at a scan rate of 5 mV s^{-1} (Table 2).

Both energy and power densities' dependence on the effective electrode area have one exception each that does not follow the same tendency (TSC_3 and TSC_2, respectively). In the case of TSC_3, the lower energy density relative to the value that would be expected can be explained by the lower specific capacitance. On the other hand, TSC_2 presents lower power density than the other devices with higher electrode areas (TSC_3 and TSC_4) due to its significantly higher R_{ES} . The Ragone plot (Fig. 6d), which allows assessing the devices in terms of energy and power densities simultaneously, reveals that the device with the smallest area, TSC_1, should be selected for applications that require fast delivering of electrical energy due to its higher power density (2.72 kW kg^{-1}), while the device with the largest area, TSC_4, should be selected for applications that demand higher amount of electrical energy due to its higher energy density (6.30 W h kg^{-1}).

In order to benchmark the energy storage performance of the TESCs prepared in this work vs. that of other textile, fabric, or fiber SCs based on carbon materials reported in the literature, the corresponding Ragone charts were plotted together and are presented in Fig. 7. Moreover, in Table 3 are summarized the respective energy density and power density outputs, grouped by SC type (EDLC or hybrid) and electrolyte type, including those of TSC_1, TSC_2, TSC_3 and TSC_4.

The energy and/or power density values of the TESCs prepared in this work surpass those of other EDLC-type fabric/cloth/fiber SCs published in the literature composed of carbon electrode materials (Table 3), including carbon nanotubes [36, 61, 62] and graphene nanosheets [63], or based on carbonized textiles/fibers [6, 64]. For instance, TSC_4 presents 1.8 times higher energy density and 20 times higher power density than an EDLC-type device based on activated carbon fiber cloth electrodes and a polymer electrolyte (poly(acrylamide)–H₂SO₄–H₂O) [64]. Additionally, TSC_1 presents 1.9 times higher energy density and 3.4 times higher power density than a SC composed of SWCNTs/polyester electrodes and a liquid electrolyte (Na₂SO₄ aqueous solution) [61], while TSC_4 delivers 2.3 times higher energy density and 1.4 times higher power density than the same SWCNT-based TESC. Concerning other works on EDLC-type TESCs based on MWCNTs, Xu et al. produced a cloth-based SC in two different

configurations (laminated and tandem structures) by coating the fabric with hydroxyl-functionalized MWCNTs through a dip-dry process [36]. Although the TESC contained functionalized MWCNTs, its energy density was significantly lower (~ 13.7 times for a single cell with tandem structure) than that achieved by TSC_4 (0.46 W h kg^{-1} vs. 6.30 W h kg^{-1}) notwithstanding the higher power density (6.81 kW kg^{-1} vs. 1.12 kW kg^{-1}).

More remarkably, when comparing with more complex hybrid TESCs, the overall performance of TSC_4 is superior to that a hybrid TESC based on nitrogen-doped graphene/polyacrylic acid/polyaniline (NG-PAA/PANI) composites coated on carbon cloth ($E = 5.8 \text{ W h kg}^{-1}$ at $P = 1.1 \text{ kW kg}^{-1}$) [65] and comparable to that of a hybrid TESC composed of MnO₂/MWCNT/textile electrodes [66]. In addition, TSC_4 presents 1.3 times higher energy density than a hybrid TESC based on MnO₂ nanorods/carbon nanoparticles hybrid nanomaterial and using carbon fabric as substrate and current collector (4.80 W h kg^{-1} vs. 6.30 W h kg^{-1}) [67] and similar energy density to that of a hybrid TESC composed of nitrogen-doped carbonized cotton (6.2 W h kg^{-1} vs. 6.30 W h kg^{-1}) [68]. On the other hand, TSC_1 exhibits 1.8 times higher power density than that of a TESC containing reduced graphene oxide nanosheets/Polyamide-66 nanofiber fabric electrodes (2.72 kW kg^{-1} vs. 1.5 kW kg^{-1}) [69]. These supercapacitors combine an EDLC-type component (carbon material) with a pseudocapacitive material (metal oxide and/or conductive polymer), while our devices are exclusively composed of carbon materials. These comparisons are highlighted in the Ragone plot of Fig. 7. In the upper-right of the Ragone plot, it is possible to identify SCs that exhibit higher outputs than the devices studied herein. They are systems that combine different types of electrode active materials, complex production techniques or require multiple coating layers, such as the hybrid SCs based on MnO₂/SWCNT/cotton [61], RuO₂ NWs/SWCNT/cloth fabric [62], ACT/Co-Al LDH//ACT/Co-Al LDH or Co-Al LDH/ACT//Graphene/ACT [70] and PPy/MWCNTs/Cotton fabric [71].

Hence, the all-solid-state flexible textile SCs reported in this work are promising SC energy storage systems since they were produced using cost-effective electrode materials and scalable processes namely: (1) commercial MWCNTs of industrial grade as electrode materials, that have lower cost, (2) a safe

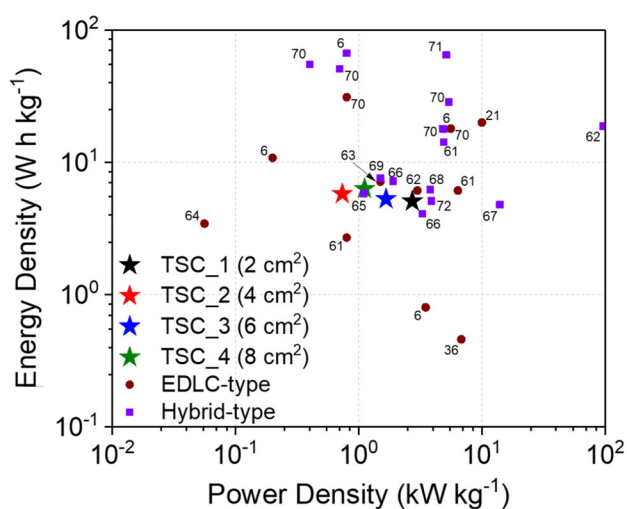


Figure 7 Ragone plot comparing the energy/power performance of all produced TESCs (TSC_1, TSC_2, TSC_3 and TSC_4) at a scan rate of 5 mV s^{-1} with that of other textile/fabric/fiber SCs based on carbon materials reported in the literature.

Table 3 Comparison of the electrochemical performance of all TESC's produced in this work with that of other flexible carbon-based fabric/fiber SCs recently reported in the literature

SC type	Electrode configuration ^a		Electrolyte	E (W h kg ⁻¹)	P (kW kg ⁻¹)	References
EDLC	MWCNT/cotton fabric	TSC_1	Solid	5.07	2.72	This work
		TSC_2		5.78	0.74	
		TSC_3		5.29	1.67	
		TSC_4		6.30	1.12	
	ACT ^b		Liquid	~ 10.8	~ 0.2	[6]
				~ 0.8	~ 3.5	
	SWCNT/cotton fabric			20	10	[21]
	SWCNT/polyester			2.7	0.8	[61]
	SWCNT/cotton			6.1	6.4	
	Graphene NSs/cotton			7.13	1.5	[63]
	MWCNT/nonwoven cloth ^c		Solid	0.46	6.81	[36]
	SWCNT/cloth fabric			6.1	3.0	[62]
	ACT/graphene//ACT/graphene ^b			~ 31.1	~ 0.8	[70]
				~ 18.0	~ 5.6	
Hybrid SCs	Activated carbon fiber cloth			3.45	0.056	[64]
	MnO ₂ /ACT//ACT ^d		Liquid	66.7	0.8	[6]
				17.8	4.97	
	MnO ₂ /SWCNT/cotton			14.2	4.9	[61]
	N-doped carbonized cotton			6.2	3.823	[68]
	rGO NSs/polyamide-66 nanofiber fabric			7.6	1.5	[69]
	MnO ₂ /MWCNT/textile ^{e,f}		Solid	7.2	1.9	[66]
				4.1	3.3	
	RuO ₂ NW/SWCNT/cloth fabric			18.8	96	[62]
	ACT/Co-Al LDH//ACT/Co-Al LDH ^{b,g}			~ 50.7	~ 0.7	[70]
				~ 18.0	~ 4.8	
	ACT/Co-Al LDH //ACT/graphene ^{b,g}			~ 54.9	~ 0.4	
				~ 28.6	~ 5.4	
	MnO ₂ /Carbon NPs/carbon fabric			4.80	14	[67]
N-Graphene-PAA/PANI/carbon cloth ^h			5.8	1.1	[65]	
			5.1	3.9		
PPy/MWCNT/cotton fabric			64.64	5.14	[71]	

^aACT activated cotton textile (carbonized cotton textile), LDH layered double hydroxide, NS nanosheet, NW nanowire, PAA polyacrylic acid, PANI polyaniline, PPy polypyrrole, rGO reduced graphene oxide

^bEstimated by figure from the cited reference

^cConsidering only one cell with $1.5 \times 1.5 \text{ cm}^2$ of effective electrode area

^dValues obtained at 1 mA cm^{-2} (first row) and 20 mA cm^{-2} (second row)

^eIn that work, besides the solid-gel electrolyte, the SC assembly required a thick filtration membrane ($200 \mu\text{m}$) as separator

^fValues obtained at current densities of 0.5 A g^{-1} (first row) and 5 A g^{-1} (second row)

^gValues obtained at 7.5 mA cm^{-2} (first row) and 50 mA cm^{-2} (second row)

^hEnergy and power density values measured by a three-electrode method

and eco-friendly solid-gel electrolyte based on PVA doped with H_3PO_4 which, when compared with other types of electrolytes, such as aqueous electrolytes or ionic liquids, imparts high flexibility, lightness, and safety to the resulting SCs, allows developing all-solid-state devices, and eliminates the

need for a separator membrane [56, 72], and (3) the conventional textile dyeing process (dip-pad-dry) to produce the fabric electrodes that mimics those already existing in the Textile Industry, but replacing the dyes by the nanomaterial ink to boost the scale-up

and implementation of our devices fabrication in the Textile Industry.

Practical operating performance

In order to explore the versatility of the produced TESC's aiming to optimize the working voltage and output current towards the target devices to be powered, two cells of TSC_3 ($1.5 \times 4 \text{ cm}^2$) were assembled in series and/or in parallel and CV and GCD tests were performed. From Figure S7A (Supplementary Material), it can be observed that the output voltage of the devices connected in series is almost twice the value obtained for a single device under similar current density conditions (4.44 V vs. 2.17 V). Furthermore, the output current of the two devices assembled in parallel is twice that of a single device (1.19 mA vs. 0.56 mA, see Figure S7B in Supplementary Material). These results probably arise from the decrease in the internal resistance to half when using the parallel configuration, thus doubling the current intensity value. On the other hand, for the parallel configuration, the maximum voltage during the charge is slightly smaller than that of the individual cell. Nevertheless, when removing the applied current, the voltage decreases to a value close to that of the single cell. Concerning the CV measurements (Figure S7B in Supplementary Material), it can be observed that in the case of the parallel configuration, the i - V cycle presents larger area ($\sim 2\times$), which is a fingerprint of the increase in the specific capacitance and of the corresponding energy density ($C_{\text{cell,parallel}} = 5.22 \text{ F g}^{-1}$ and $E_{\text{parallel}} = 2.56 \text{ W h kg}^{-1}$ at a scan rate of 1 mV s^{-1}). These results confirm that the output voltage and current intensity can be tailored through the distinct coupling of single textile SC cells in order to match the technical specifications of the device to be powered.

Finally, to assess the potentialities of the produced TESC's to power commercial electronic gadgets and validate their practical operating performance, a commercial temperature and hygrometer sensor system was tested, measuring the sensor operation time. The load of each TESC was of 60 s with an applied current of 2 mA, and the results are displayed in Fig. 8.

Concerning single cells, a linear increase in the sensor operating time can be observed upon the increase in the area of the device, reaching ~ 13 min for the device with the largest area (8 cm^2). It is

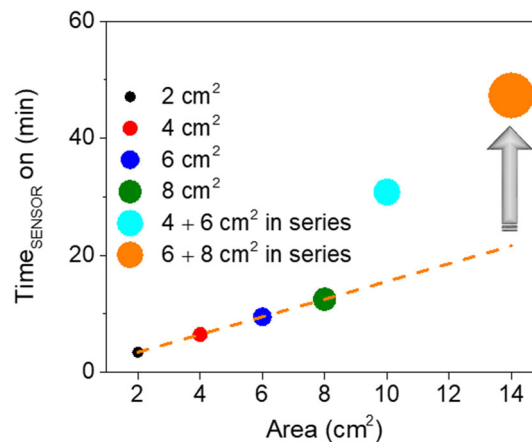


Figure 8 Influence of the electrode active area on the real performance of the TESC's to power a digital thermometer/hygrometer sensor.

noteworthy that by coupling two TESC's in series to increase the voltage value (as previously discussed), in this case TSC_3 and TSC_4, it is possible to power the device for up to 47 min, corresponding to a total electrode active area of 14 cm^2 . More impressively, the coupled TESC's allow reaching a total sensor operating time more than twice the value that would be reached with a single cell of 14 cm^2 (~ 22 min, extrapolation line in Fig. 8). A similar trend can be observed when coupling TSC_2 and TSC_3 in series, corresponding to a total electrode area of 10 cm^2 .

The produced TESC's were also efficient energy storage systems to supply LEDs, a heart rate monitor, and a pedometer during several minutes when coupled in series and/or in parallel (Fig. 9 and Movies 1 and 2 in the Supplementary Material).

In summary, the MWCNT-based TESC's produced in this work offer good guarantee of application to power wearable devices since with only 2, 3, or 4 SC's connected in series and/or in parallel it was possible to power the aforementioned wearable electronic devices. Hence, they meet the energy and power requirements of portable electronics under real conditions. Then we can anticipate that with a garment of medium size with a surface area of approximately 7632 cm^2 , which allows incorporating more than 3500 SC units, we will achieve a total energy of 0.042 Wh or 20.10 mAh and a total power of 22.47 W to power wearable devices.

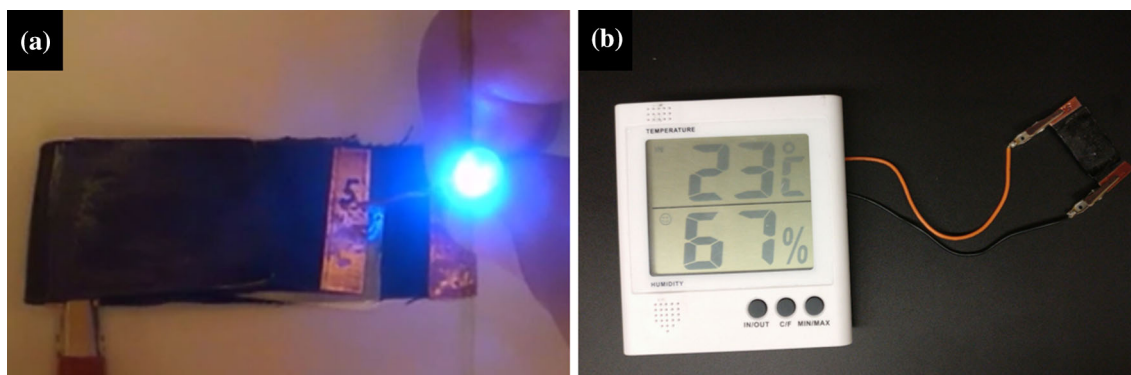


Figure 9 Proof-of-concept optical photographs of the practical operating performance of the produced TESC: **a** LED powered by a textile device composed of two TSC_3 cells ($1.5 \times 4 \text{ cm}^2$)

connected in series; and **b** digital thermometer/hygrometer sensor powered by one TSC_3 cell.

Conclusions

In summary, efficient and durable all-solid-state TESC of different dimensions were directly produced on fabrics using cost-effective industrial grade MWCNTs as electrode material and a safe and eco-friendly solid-gel polyelectrolyte. A readily-available natural textile substrate (cotton) and the scalable eco-sustainable dip-pad-dry textile dyeing process were used for the fabrication of the textile electrodes, aiming to boost the technological transfer and implementation of the SCs fabrication in the Textile Industry.

The electrochemical performance could be tuned by changing the geometrical features of the textile electrode and the active area of the SC: the maximum energy density was achieved for the TESC with the largest area, while the highest power density was achieved for the smallest TESC, reaching 6.30 W h kg^{-1} and 2.72 kW kg^{-1} at 5 mV s^{-1} , respectively. These values surpassed those of other EDLC-type carbon-based fabric/cloth SCs. Moreover, they were comparable to those of some hybrid devices produced by more complex and time-consuming processes that pose constraints towards industrial production.

Hence, this work constitutes an advance on the understanding of the role of the textile electrode features on the energy storage properties of the resulting textile SCs, towards the architected design of wearable SCs with enhanced performance.

Supplementary material available

Complementary EDS and TEM characterization (Figures S1 and S2). Schematic representation of the process used to produce the TESC (Figure S3) and complementary SCs electrochemical characterization (Figures S4, S5, S6 and S7). Video clips of the as-produced TESC powering a digital thermometer/hygrometer sensor (Movie 1) and an array of LEDs (Movie 2).

Acknowledgements

This work was funded by FEDER—European Regional Development Fund through COMPETE 2020—Operacional Programme for Competitiveness and Internationalization (POCI) and by Portuguese funds through Fundação para a Ciência e a Tecnologia (FCT)/MCTES under Program PT2020 in the framework of the projects PTDC/CTM-TEX/31271/2017, UIDB/50006/2020 and UIDB/04968/2020. R.S.C. thanks for the grant funding from the European Union's Horizon 2020 Research and Innovation Programme under Grant Agreement No. 863307. C.P. thanks FCT for the FCT Investigator contract IF/01080/2015.

Compliance with ethical standards

Conflict of interest The authors declare that they have no conflict of interest.

Electronic supplementary material: The online version of this article (<https://doi.org/10.1007/s108>

53-020-04709-0) contains supplementary material, which is available to authorized users.

References

- [1] Li C, Islam MM, Moore J et al (2016) Wearable energy-smart ribbons for synchronous energy harvest and storage. *Nat Commun* 7:13319–13329
- [2] Jost K, Dion G, Gogotsi Y (2014) Textile energy storage in perspective. *J Mater Chem A* 2:10776–10787
- [3] Huang Q, Wang D, Zheng Z (2016) Textile-based electrochemical energy storage devices. *Adv Energy Mater* 6:1600783–1600811
- [4] Gulzar U, Goriparti S, Miele E et al (2016) Next-generation textiles: from embedded supercapacitors to lithium ion batteries. *J Mater Chem A* 4:16771–16800
- [5] Wu Z, Li L, Yan J, Zhang X (2017) Materials design and system construction for conventional and new-concept supercapacitors. *Adv Sci* 4:1600382–1600430
- [6] Bao L, Li X (2012) Towards textile energy storage from cotton T-Shirts. *Adv Mater* 24:3246–3252
- [7] Jiang Y, Ling X, Jiao Z et al (2015) Flexible of multiwalled carbon nanotubes/manganese dioxide nanoflake textiles for high-performance electrochemical capacitors. *Electrochim Acta* 153:246–253
- [8] Yuksel R, Unalan HE (2015) Textile supercapacitors-based on MnO₂/SWNT/conducting polymer ternary composites. *Int J Energy Res* 39:2042–2052
- [9] Dong L, Liang G, Xu C et al (2017) Multi hierarchical construction-induced superior capacitive performances of flexible electrodes for wearable energy storage. *Nano Energy* 34:242–248
- [10] Liu C, Cai Z, Zhao Y et al (2016) Potentiostatically synthesized flexible polypyrrole/multi-wall carbon nanotube/cotton fabric electrodes for supercapacitors. *Cellulose* 23:637–648
- [11] Zhou M, Zhang H, Qiao Y et al (2018) A flexible sandwich-structured supercapacitor with poly(vinyl alcohol)/H₃PO₄-soaked cotton fabric as solid electrolyte, separator and supporting layer. *Cellulose* 25:3459–3469
- [12] Ye X, Zhou Q, Jia C et al (2016) A knittable fibriform supercapacitor based on natural cotton thread coated with graphene and carbon nanoparticles. *Electrochim Acta* 206:155–164
- [13] Huang G, Hou C, Shao Y et al (2015) High-performance all-solid-state yarn supercapacitors based on porous graphene ribbons. *Nano Energy* 12:26–32
- [14] Zhou Q, Jia C, Ye X et al (2016) A knittable fiber-shaped supercapacitor based on natural cotton thread for wearable electronics. *J Power Sources* 327:365–373
- [15] Zhang X, Lai Y, Ge M et al (2015) Fibrous and flexible supercapacitors comprising hierarchical nanostructures with carbon spheres and graphene oxide nanosheets. *J Mater Chem A* 3:12761–12768
- [16] Sun J, Huang Y, Fu C et al (2016) High-performance stretchable yarn supercapacitor based on PPy@CNTs@urethane elastic fiber core spun yarn. *Nano Energy* 27:230–237
- [17] Zhang C, Chen Z, Rao W et al (2019) A high-performance all-solid-state yarn supercapacitor based on polypyrrole-coated stainless steel/cotton blended yarns. *Cellulose* 26:1169–1181
- [18] Singha K (2012) A review on coating and lamination in textiles: processes and applications. *Am J Polym Sci* 2:39–49
- [19] Schindler WD, Hauser PJ (2004) Chemical finishing of textiles, 1st edn. Woodhead Publishing Ltd, Cambridge, England
- [20] Liu W, Song M-S, Kong B, Cui Y (2017) Flexible and stretchable energy storage: recent advances and future perspectives. *Adv Mater* 29:1603436–1603470
- [21] Hu L, Pasta M, La Mantia F et al (2010) Stretchable, porous, and conductive energy textiles. *Nano Lett* 10:708–714
- [22] Chee WK, Lim HN, Zainal Z et al (2016) Flexible graphene-based supercapacitors: a review. *J Phys Chem C* 120:4153–4172
- [23] Sun H, Xie S, Li Y et al (2016) Large-area supercapacitor textiles with novel hierarchical conducting structures. *Adv Mater* 28:8431–8438
- [24] Zhao X, Sánchez BM, Dobson PJ, Grant PS (2011) The role of nanomaterials in redox-based supercapacitors for next generation energy storage devices. *Nanoscale* 3:839–855
- [25] Aricò AS, Bruce P, Scrosati B et al (2005) Nanostructured materials for advanced energy conversion and storage devices. *Nat Mater* 4:366–377
- [26] Zhang C, Tian J, Rao W et al (2019) Polypyrrole@metal-organic framework (UIO-66)@cotton fabric electrodes for flexible supercapacitors. *Cellulose* 26:3387–3399
- [27] Bo Y, Zhao Y, Cai Z et al (2018) Facile synthesis of flexible electrode based on cotton/polypyrrole/multi-walled carbon nanotube composite for supercapacitors. *Cellulose* 25:4079–4091
- [28] Staaf LGH, Lundgren P, Enoksson P (2014) Present and future supercapacitor carbon electrode materials for improved energy storage used in intelligent wireless sensor systems. *Nano Energy* 9:128–141
- [29] Cheng Y, Liu J (2013) Carbon nanomaterials for flexible energy storage. *Mater Res Lett* 1:175–192

- [30] Pandolfo AG, Hollenkamp AF (2006) Carbon properties and their role in supercapacitors. *J Power Sour* 157:11–27
- [31] Zhang LL, Zhao XS (2009) Carbon-based materials as supercapacitor electrodes. *Chem Soc Rev* 38:2520–2531
- [32] Zhang M, Annamalai KP, Liu L et al (2016) A mini review over the applications of nano-carbons and their composites in supercapacitors. *Recent Innov Chem Eng* 9:4–19
- [33] Hao T, Sun J, Wang W, Yu D (2018) MWCNTs-COOH/cotton flexible supercapacitor electrode prepared by improvement one-time dipping and carbonization method. *Cellulose* 25:4031–4041
- [34] Pasta M, La Mantia F, Hu L et al (2010) Aqueous supercapacitors on conductive cotton. *Nano Res* 3:452–458
- [35] Charitidis C, Georgiou P, Koklioti M et al (2014) Manufacturing nanomaterials: from research to industry. *Manuf Rev* 1:11–30
- [36] Xu J, Wu H, Xu C et al (2013) Structural engineering for high energy and voltage output supercapacitors. *Chem A Eur J* 19:6451–6458
- [37] Yu G, Hu L, Vosgueritchian M et al (2011) Solution-processed graphene/MnO₂ nanostructured textiles for high-performance electrochemical capacitors. *Nano Lett* 11:2905–2911
- [38] Fang L, Zhang X, Sun D (2013) Chemical modification of cotton fabrics for improving utilization of reactive dyes. *Carbohydr Polym* 91:363–369
- [39] Klemm D, Heublein B, Fink H-P, Bohn A (2005) Cellulose: fascinating biopolymer and sustainable raw material. *Angew Chemie Int Ed* 44:3358–3393
- [40] Yao X, Kou X, Qiu J (2016) Multi-walled carbon nanotubes/polyaniline composites with negative permittivity and negative permeability. *Carbon* 107:261–267
- [41] Liang Y, Weng W, Yang J et al (2017) Asymmetric fabric supercapacitor with a high areal energy density and excellent flexibility. *RSC Adv* 7:48934–48941
- [42] Lehman JH, Terrones M, Mansfield E et al (2011) Evaluating the characteristics of multiwall carbon nanotubes. *Carbon* 49:2581–2602
- [43] Rebelo SLH, Guedes A, Szeferczyk ME et al (2016) Progress in the Raman spectra analysis of covalently functionalized multiwalled carbon nanotubes: Unraveling disorder in graphitic materials. *Phys Chem Chem Phys* 18:12784–12796
- [44] Qi H, Liu J, Mäder E (2014) Smart cellulose fibers coated with carbon nanotube networks. *Fibers* 2:295–307
- [45] Cabrales L, Abidi N, Manciu F (2014) Characterization of developing cotton fibers by confocal Raman microscopy. *Fibers* 2:285–294
- [46] Adebajo MO, Frost RL, Klopogge JT, Kokot S (2006) Raman spectroscopic investigation of acetylation of raw cotton. *Spectrochim Acta - Part A Mol Biomol Spectrosc* 64:448–453
- [47] Zhang S, Pan N (2015) Supercapacitors performance evaluation. *Adv Energy Mater* 5:1401401–1401420
- [48] Zhang J, Zhao XS (2012) On the configuration of supercapacitors for maximizing electrochemical performance. *Chemsuschem* 5:818–841
- [49] Mei BA, Munteshari O, Lau J et al (2018) Physical interpretations of nyquist plots for EDLC electrodes and devices. *J Phys Chem C* 122:194–206
- [50] Taberna PL, Simon P, Fauvarque JF (2003) Electrochemical characteristics and impedance spectroscopy studies of carbon-carbon supercapacitors. *J Electrochem Soc* 150:A292–A300
- [51] Ujjain SK, Bhatia R, Ahuja P, Attri P (2015) Highly conductive aromatic functionalized multi-walled carbon nanotube for inkjet printable high performance supercapacitor electrodes. *PLoS ONE* 10:e0131475–e0131487
- [52] Kumar N, Ginting RT, Kang J-W (2018) Flexible, large-area, all-solid-state supercapacitors using spray deposited PEDOT:PSS/reduced-graphene oxide. *Electrochim Acta* 270:37–47
- [53] Chen L, Ji T, Mu L, Zhu J (2017) Cotton fabric derived hierarchically porous carbon and nitrogen doping for sustainable capacitor electrode. *Carbon* 111:839–848
- [54] He M, Fic K, Frackowiak E et al (2016) Ageing phenomena in high-voltage aqueous supercapacitors investigated by in situ gas analysis. *Energy Environ Sci* 9:623–633
- [55] Barzegar F, Dangbegnon JK, Bello A et al (2015) Effect of conductive additives to gel electrolytes on activated carbon-based supercapacitors. *AIP Adv* 5:097171–097180
- [56] Gao Z, Song N, Zhang Y, Li X (2015) Cotton textile enabled, all-solid-state flexible supercapacitors. *RSC Adv* 5:15438–15447
- [57] Lukatskaya MR, Dunn B, Gogotsi Y (2016) Multidimensional materials and device architectures for future hybrid energy storage. *Nat Commun* 7:12647–12660
- [58] Béguin F, Presser V, Balducci A, Frackowiak E (2014) Carbons and electrolytes for advanced supercapacitors. *Adv Mater* 26:2219–2251
- [59] Jost K, Perez CR, McDonough JK et al (2011) Carbon coated textiles for flexible energy storage. *Energy Environ Sci* 4:5060–5067
- [60] González A, Goikolea E, Barrena JA, Mysyk R (2016) Review on supercapacitors: Technologies and materials. *Renew Sustain Energy Rev* 58:1189–1206
- [61] Yun TG, Oh M, Hu L et al (2013) Enhancement of electrochemical performance of textile based supercapacitor using mechanical pre-straining. *J Power Sour* 244:783–791

- [62] Chen P, Chen H, Qiu J, Zhou C (2010) Inkjet printing of single-walled carbon nanotube/RuO₂ nanowire supercapacitors on cloth fabrics and flexible substrates. *Nano Res* 3:594–603
- [63] Liu W, Yan X, Lang J et al (2012) Flexible and conductive nanocomposite electrode based on graphene sheets and cotton cloth for supercapacitor. *J Mater Chem* 22:17245–17253
- [64] Stepniak I, Ciszewski A (2011) Electrochemical characteristics of a new electric double layer capacitor with acidic polymer hydrogel electrolyte. *Electrochim Acta* 56:2477–2482
- [65] Wang Y, Tang S, Vongehr S et al (2016) High-performance flexible solid-state carbon cloth supercapacitors based on highly processible N-graphene doped polyacrylic acid/polyaniline composites. *Sci Rep* 6:12883–12893
- [66] Ko W-Y, Chen Y-F, Lu K-M, Lin K-J (2016) Porous honeycomb structures formed from interconnected MnO₂ sheets on CNT-coated substrates for flexible all-solid-state supercapacitors. *Sci Rep* 6:18887–18894
- [67] Yuan L, Lu X-H, Xiao X et al (2012) Flexible solid-state supercapacitors based on carbon nanoparticles/MnO₂ nanorods hybrid structure. *ACS Nano* 6:656–661
- [68] Li L, Zhong Q, Kim ND et al (2016) Nitrogen-doped carbonized cotton for highly flexible supercapacitors. *Carbon* 105:260–267
- [69] Wang YS, Li SM, Hsiao ST et al (2014) Integration of tailored reduced graphene oxide nanosheets and electrospun polyamide-66 nanofabrics for a flexible supercapacitor with high-volume- and high-area-specific capacitance. *Carbon* 73:87–98
- [70] Gao Z, Bumgardner C, Song N et al (2016) Cotton-textile-enabled flexible self-sustaining power packs via roll-to-roll fabrication. *Nat Commun* 7:11586–11597
- [71] Huang S, Chen P, Lin W et al (2016) Electrodeposition of polypyrrole on carbon nanotube-coated cotton fabrics for all-solid flexible supercapacitor electrodes. *RSC Adv* 6:13359–13364
- [72] Gu W, Yushin G (2014) Review of nanostructured carbon materials for electrochemical capacitor applications: advantages and limitations of activated carbon, carbide-derived carbon, zeolite-templated carbon, carbon aerogels, carbon nanotubes, onion-like carbon, and graphene. *Wiley Interdiscip Rev Energy Environ* 3:424–473

Publisher's Note Springer Nature remains neutral with regard to jurisdictional claims in published maps and institutional affiliations.